Single-shot spiral imaging at 7 T

Engel, Maria ; Kasper, Lars ; Barmet, Christoph ; Schmid, Thomas ; Vionnet, Laetitia ; Wilm, Bertram ; Pruessmann, Klaas P

Abstract: Purpose The purpose of this work is to explore the feasibility and performance of single-shot spiral MRI at 7 T, using an expanded signal model for reconstruction. Methods Gradient-echo brain imaging is performed on a 7 T system using high-resolution single-shot spiral readouts and half-shot spirals that perform dual-image acquisition after a single excitation. Image reconstruction is based on an expanded signal model including the encoding effects of coil sensitivity, static off-resonance, and magnetic field dynamics. The latter are recorded concurrently with image acquisition, using NMR field probes. The resulting image resolution is assessed by point spread function analysis. Results Single-shot spiral imaging is achieved at a nominal resolution of 0.8 mm, using spiral-out readouts of 53-ms duration. High depiction fidelity is achieved without conspicuous blurring or distortion. Effective resolutions are assessed as 0.8, 0.94, and 0.98 mm in CSF, gray matter and white matter, respectively. High image quality is also achieved with half-shot acquisition yielding image pairs at 1.5-mm resolution. Conclusion Use of an expanded signal model enables single-shot spiral imaging at 7 T with unprecedented image quality. Single-shot and half-shot spiral readouts deploy the sensitivity benefit of high field for rapid high-resolution imaging, particularly for functional MRI and arterial spin labeling.

DOI: https://doi.org/10.1002/mrm.27176

Single-shot spiral imaging at 7T

Maria Engel[1], Lars Kasper[1,2], Christoph Barmet[1,3], Thomas Schmid[1], Bertram Wilm[1,3], Klaas P Pruessmann[1]

[1]Institute for Biomedical Engineering, ETH Zurich and University of Zurich, Zurich, Switzerland

[2]Translational Neuromodeling Unit, IBT, University of Zurich and ETH Zurich, Zurich, Switzerland

[3]Skope Magnetic Resonance Technologies AG, Zurich, Switzerland

Corresponding author: Klaas P Pruessmann, Ph.D., Institute for Biomedical Engineering, ETH Zurich and University of Zurich, ETZ F 89, Gloriastrasse 35, 8092 Zurich, Switzerland. E-mail: pruessmann@biomed.ee.ethz.ch

Word count: 4322

Institution: Institute for Biomedical Engineering, ETH Zurich and University of Zurich, Zurich, Switzerland

Running title: Single-shot spiral imaging at 7T

Abstract

Purpose

The purpose of this work is to explore the feasibility and performance of single-shot spiral MRI at 7T, using an expanded signal model for reconstruction.

Methods

Gradient-echo brain imaging is performed on a Philips Achieva 7T system, using high-resolution single-shot spiral readouts as well as half-shot spirals that perform dual image acquisition after a single excitation. Image reconstruction is based on an expanded signal model including the encoding effects of coil sensitivity, static off-resonance, and magnetic field dynamics. The latter are recorded concurrently with image acquisition, using NMR field probes. Resulting image resolution is assessed by PSF analysis.

Results

Single-shot spiral imaging is achieved at a nominal resolution of 0.8 mm, using spiral-out readouts of 53 ms duration. High depiction fidelity is achieved without conspicuous blurring or distortion. Effective resolutions are assessed as 0.8 mm, 0.94 mm, and 0.98 mm in CSF, gray matter and white matter, respectively. High image quality is also achieved with half-shot acquisition yielding image pairs at 1.5 mm resolution.

Conclusion

Use of an expanded signal model enables single-shot spiral imaging at 7T with unprecedented image quality. Single-shot and half-shot spiral readouts deploy the sensitivity benefit of high field for rapid high-resolution imaging, particularly for fMRI and ASL.

Key words: single-shot spiral; magnetic field monitoring; algebraic image reconstruction; spiral imaging

Introduction

Image encoding in MRI is performed with a large variety of strategies for traversing k-space. Among these, spiral readouts stand out in terms of time efficiency and average k-space speed that can be achieved within given gradient amplitude and slew-rate constraints (1–3). Single-shot spiral trajectories, in particular, rank among the fastest ways of covering k-space for given resolution and FOV (4). Center-out spirals permit shorter echo times than echo-planar scanning and offer relative robustness against flow artifacts since their first gradient moments are zero in the k-space center and continue to be nulled once per turn of the trajectory (2,3,5). These properties render single-shot spiral acquisition attractive for a number of purposes such as diffusion-weighted imaging (6,7), arterial spin labeling (ASL) (8), and BOLD fMRI (4,9). In fMRI, spiral readouts have even been used for acquisition of two images per shot, performing successive inward and outward spirals after a single excitation (10,11).

However, to-date spiral readouts have not been widely deployed in applied studies due mostly to two issues. Firstly, spiral imaging is particularly sensitive to imperfections of magnetic field dynamics, which give rise to blurring, distortion, and other artifacts when unaddressed (3,12). Deviations from nominal field dynamics arise primarily from low-pass behavior of gradient chains, delays, eddy currents (13,14), and concomitant fields (15). They may also involve anisotropic system response (16), thermal drift (17,18) and mechanical vibrations (19), as well as dynamic susceptibility effects, e.g., due to breathing (20–22). The chief traditional means of addressing these issues are delay calibration (3), gradient pre-emphasis (23), and measurement of effective k-space trajectories (3,24,25) for use in Fourier reconstruction. In recent years, dynamic field imperfections have also been tackled by concurrent field recordings and field models of higher spatial order (26).

The second principal challenge in spiral imaging is static off-resonance, which arises from magnetic field non-uniformity as well as chemical shift. Off-resonance causes phase errors that scale with readout duration and are thus particularly limiting for single-shot acquisition (3,12,27). When unaddressed, with spiral readouts they give rise to PSF broadening and thus to blurring in resulting images. This problem can be mitigated by parallel imaging with k-space undersampling and array detection (28–32), however at the expense of SNR. At the reconstruction level, off-resonance is most commonly countered by conjugate-phase reconstruction, which works within certain limits on how rapidly frequency offsets may vary in space (33–36). More general cases have been tackled with iterative reconstruction algorithms for full-Fourier encoding (37–39) and parallel imaging (40). To address static and dynamic field perturbations jointly, image reconstruction has recently been

performed by inversion of an expanded signal model incorporating the encoding effects of both as well as those of array detection (26).

Using an expanded signal model, single-shot spiral imaging with promising image quality has recently been reported for 3 T (7,41), achieving 1.3 mm in-plane resolution in the brain with readouts of 32 ms. Such readout specifications are suited for diffusion imaging and BOLD fMRI at intermediate field strength and voxel size. However, single-shot readouts are equally attractive at higher main field and resolution, particularly for BOLD fMRI and ASL, which benefit greatly from enhanced baseline sensitivity (42,43). At 7T, spiral imaging has only been reported with segmented readouts up to 20 ms, targeting structural contrast (44,45). Towards single-shot high-resolution acquisition at 7T, the main obstacle is that high field exacerbates the off-resonance challenge. Higher fields tend to be less uniform since susceptibility effects scale with field strength. Additionally, off-resonance phase accrual increases as readouts grow longer for higher resolution.

The purpose of the present work is to take on this challenge and explore the feasibility of single-shot spiral acquisition at high field. Brain imaging with T_2* contrast is performed at 7T, using the expanded-model approach for reconstruction. Single-shot 2D imaging is accomplished with 0.8 mm nominal in-plane resolution, relying on extended readouts of 53 ms in length. In addition, long-readout capability is deployed for dual-image acquisition with successive inward and outward spirals.

Methods

Setup

All experiments were carried out on a 7T Achieva system (Philips Healthcare, Best, The Netherlands) using a quadrature-transmit and 32-channel head receive array (Nova Medical, Wilmington, USA). The system was operated in a mode offering a maximum gradient amplitude of 31 mT/m at maximum slew rate of 200 T/m/s on all axes simultaneously. For field recordings, an array of 16 fluorine NMR field probes (hexafluorobenzene, T_1 = 86 ms, T_2^* = 24 ms) (3,46–48) were integrated in the head setup. The probes were mounted on a laser-sintered nylon frame between the transmit coil and the receive array (Fig. 1). The probe positions on the frame were determined by joint minimization of radiofrequency (RF) interaction with the volume transmitter and noise propagation from probe signals into spherical harmonic field expansions. At a droplet diameter of 800 µm, the probes were suitable for k-space excursions up to the equivalent of 400 µm resolution. The field-recording setup was operated with the transmit/receive chains and console hardware described in Ref. (49). Data were collected from healthy volunteers according to the applicable ethics regulation.

Spiral sequences

Archimedean spiral readouts were incorporated in a multi-slice 2D gradient echo sequence (Fig. 2). The spiral gradient waveforms were computed such as to minimize their duration within gradient-strength and slew-rate constraints (50). The radial spacing of spiral turns was set such as to undersample k-space by a factor of 4 with respect to the field of view of 23 cm. Upon repetition each trajectory was rotated by increments of 90° such that four successive acquisitions jointly amounted to full Fourier sampling. Table 1 lists further parameters of three specific trajectory implementations sketched in Figure 2. The first of these, targeting high resolution, was a center-out spiral with a nominal in-plane resolution of 0.8 mm (35 spiral revolutions per shot) used to read out slices of 1 and 2 mm thickness. In the second and third examples, lower-resolution (1.5 mm in-plane, 2 mm slices, 20 spiral revolutions per half-shot) outward and inward spirals were concatenated in either order, forming spiral-in-out and spiral-out-in schemes. Acquiring two images after a single excitation, these readouts will also be referred to as *half-shot* spirals in the following. In the spiral-in-out case, a suitable pre-phasing gradient was included before the inward part. Throughout, slice excitation was preceded by a SPIR module (51) to suppress fat signal from the scalp (not shown in the sequence diagram). The whole brain was covered by 36 equidistant, transverse slices, resulting in a slice repetition time of 3.3 s.

Field recording

The field probes were excited just before the start of the spiral waveforms and read out concurrently with image acquisition (Fig. 2). Field recording was performed for every third slice and interpolated for adjacent slices, allowing near-complete probe recovery between excitations. The phase time courses of acquired probe signals were used to calculate a time-resolved field expansion in terms of 2nd-order spherical harmonics (25). Second-order concomitant field effects were estimated based on the dominant 1st-order harmonics (15). The probe phase time courses were then corrected for the estimated concomitant field contributions before re-fitting the harmonic model (41).

Image reconstruction

Image reconstruction was based on the expanded signal model detailed in Refs. (7,26). In the absence of diffusion gradients, higher order eddy-current effects were assumed to be negligible as previously observed in Ref. (45) for the same system. The resulting first-order model reads

$$s_\gamma(t) = \int_V m(\boldsymbol{r})\, e^{i\,(k_0(t)+\boldsymbol{k}(t)\cdot\boldsymbol{r})}\, e^{i\,\Delta\omega_0(\boldsymbol{r})\,t}\, c_\gamma(\boldsymbol{r})\, dV \qquad [1]$$

with static frequency offset $\Delta\omega_0$, sensitivity c_γ and signal s_γ of coil γ, initial transverse magnetization m, and position vector $\boldsymbol{r} = [x\ y\ z]^T$ within the imaging volume V. k_0 and $\boldsymbol{k} = [k_x\ k_y\ k_z]^T$ describe phase accrual due to 0th- and first-order components of the recorded dynamic field expansion.

Discretization of space and time according to the targeted resolution and the acquisition bandwidth translates equation [1] into

$$\tilde{s}_{(\gamma,\tau)} = \sum_\rho E_{(\gamma,\tau),\rho}\, m_\rho, \qquad [2]$$

where the indices ρ and τ count voxels and sampling time points, respectively, $m_\rho = m(\boldsymbol{r}_\rho)$, and E denotes the encoding matrix with entries

$$E_{(\gamma,\tau),\rho} = e^{i\,\boldsymbol{k}(t_\tau)\cdot(\boldsymbol{r}_\rho - \boldsymbol{r}_0)}\, e^{i\Delta\omega_0(\boldsymbol{r}_\rho)\,t_\tau}\, c_\gamma(\boldsymbol{r}_\rho). \qquad [3]$$

In this notation, geared to 2D imaging, 0th-order field and gradients orthogonal to the image plane are accounted for by initial signal demodulation:

$$\tilde{s}_{(\gamma,\tau)} = e^{-i\,(k_0(t_\tau) + \boldsymbol{k}(t_\tau)\cdot\boldsymbol{r}_0)}\, s_{(\gamma,\tau)} \qquad [4]$$

in which $s_{(\gamma,\tau)} = s_\gamma(t_\tau)$ and $\boldsymbol{r}_0$ points to the center of the slice and field of view. In matrix-vector form, the signal model then reads

$$\tilde{\boldsymbol{s}} = E\,\boldsymbol{m}\,. \qquad [5]$$

Inversion of equation 5 is performed by conjugate-gradient iteration (28). Matrix-vector multiplications in the CG loop were accelerated by use of FFT enabled by forward and reverse gridding (28) and multiple-frequency interpolation (7,36,40). Image reconstruction was performed on a 32-node CPU cluster using Matlab (The MathWorks, Natick, MA) and critical routines implemented in C.

Maps of $\Delta\omega_0$ (Fig. 3) and coil sensitivity were calculated from a separate fat-suppressed Cartesian gradient-echo scan with full Fourier encoding and multiple echoes. The Cartesian gradient-echo images were reconstructed in the same way as described above, however neglecting off-resonance and coil sensitivity. The former was negligible due to large bandwidth of the Cartesian gradient-echo scan. Ignoring coil sensitivity resulted in separate sensitivity-weighted images per receive coil. Raw $\Delta\omega_0$ maps were obtained by pixel-wise fitting of phase evolution over the different echo times. Coil

sensitivity maps were obtained from the first-echo data dividing single-coil images by the root-sum-of-squares across the array. Both types of maps were refined by smoothing and slight extrapolation using a variational approach penalizing roughness along with deviations from the original (52). In reconstructed images, residual weighting by net array sensitivity was removed by bias-field correction (SPM12, http://www.fil.ion.ucl.ac.uk/spm/software/spm12/), which is based on an automatic segmentation approach detailed in Ref. (53).

To study the impact of the different encoding terms in the signal model, the high-resolution spiral-out data were also reconstructed based on the nominal dynamic field evolution ($k_0(t) = 0$, nominal k-space trajectory) and/or neglecting off-resonance. To illustrate the impact of parallel imaging, single-shot results are compared with reconstruction from fully Fourier-encoded data obtained with four shots.

T_2* decay during center-out spiral readouts reduces spatial resolution by radial signal attenuation in k-space. To assess the extent of this effect, the point spread function (PSF) was determined for single-shot spiral-out acquisitions based on the high-resolution trajectory specified above. Besides the full trajectory of 53 ms, fragments of length between 10 ms and 50 ms were created by truncation, using 5 ms increments. PSFs were obtained by emulating signal acquisition and image reconstruction for a point source at the center of the FOV. Array signals from a point source were synthesized by equation [1] and then attenuated by T_2* decay. T_2* values were taken from (54), which reports 33.2 ms (gray matter) and 26.8 ms (white matter) for human brain at 7T. Reconstruction was performed as described above, yielding PSFs on the image grid. For PSF analysis, the spatial representation was refined by a factor of 10 in both dimensions, using zero-padding in the Fourier domain.

Results

Single-shot spirals

Figure 4 shows the results of the high-resolution study, yielding single-shot images of 0.8 mm nominal resolution based on readouts of 53 ms each. In the top panel, five selected slices of the data set with 2 mm slice thickness are displayed. Based on spiral-out trajectories starting at an echo time (TE) of 25 ms, the data exhibits T_2^* contrast similar to typical acquisitions in BOLD fMRI. It achieves sharp delineation of tissue borders, particularly between gray and white matter as well as between brain parenchyma and cerebrospinal fluid (CSF). Notably, the obtained images do not exhibit the issues that have traditionally been associated with spiral imaging. Despite high field and very long

readouts they are not conspicuously blurred or distorted. In two slices a hypointense feature is visible between the frontal lobes. This has been confirmed to reflect a calcification of the falx cerebri, a non-pathogenic variation within the healthy population that is equally visible in the Cartesian pre-scans. In the shown data, it caused intra-voxel dephasing, which is a consequence of the long TE rather than the readout strategy. Corresponding results obtained with 1 mm slice thickness are shown in the second panel of Figure 4, along with smaller displays over a larger slice range. As expected, smaller voxel volume in these scans yields noticeably lower SNR. At the same time, the thinner slices appear slightly sharper, especially at gray-white-matter and brain-CSF interfaces. Overall, high quality of depiction at still considerable SNR is accomplished in the thinner slices.

Figure 5 shows underlying time courses of the recorded phase coefficients k_l for one slice. The 0^{th}-order coefficient is plotted in the top panel. The 1^{st}-order coefficients in the middle reflect the common k-space trajectory. The bottom graph shows the 2^{nd}-order coefficients, which were neglected in image reconstruction.

The results of varying the signal model are displayed in Figure 6, based on 1 mm slices. The panel on the left compares reconstructions from four-shot, fully Fourier-encoded data, ignoring coil sensitivity in the signal model. Assuming nominal field evolution deteriorated image quality substantially, mostly by blurring and general corruption of edges and contours. The appearance of these artefacts hardly changes upon including off-resonance in the signal model. The effect of the latter is more apparent when relying on recorded field evolution. In this case, accounting for $\Delta\omega_0$ visibly counters typical off-resonance effects such as blurring, signal pile-up, and distortion, most so in regions close to the surface where resonance offsets tend to be the largest. The benefit of accounting for coil sensitivity, finally, is illustrated by moving from full Fourier encoding to single-shot data with four-fold undersampling and array reconstruction (Fig. 6, right panel).

The results of the PSF study are shown in Figure 7. As the acquisition duration increases, nominal resolution improves approximately as the inverse square-root of acquisition time, reflecting the square dependence of the net k-space area on the k-space radius. At the level of PSFs, a convenient resolution metric is the full width at half-maximum (FWHM), which is approximately 1.4 times the nominal resolution. Neglecting T_2* decay, the FWHM reaches 1.12 mm at the full readout length of 53 ms, corresponding to 0.8 mm resolution. In gray and white matter, finite T_2* causes the FWHM to improve more slowly, reaching 1.32 mm and 1.38 mm, respectively, which correspond to resolutions of 0.94 mm and 0.98 mm. The benefit of increasing the readout duration further is reflected by the final slope of the FWHM plots. For gray and white matter this slope is approximately 2/3 of that

obtained without T_2* decay. In cerebrospinal fluid, T_2* is much longer than the acquisition times considered here and thus hardly impairs the nominal resolution.

Half-shot spirals

Figure 8 and 9 display results of half-shot imaging, obtained by separate reconstruction from the inward and outward parts of the double spirals. Figure 8 shows spiral-in-out imaging, yielding two images per slice that exhibit similar contrast since the sub-trajectories visit the center of k-space at the same time. They differ somewhat in sharpness of contours, which the second spiral depicts blurrier around the scalp but sharper between CSF and white matter due to the long T_2* of the former. The later acquisitions also exhibit stronger attenuation of residual fat signal and somewhat more pronounced signal drop-out due to dephasing in voxels exposed to susceptibility gradients. Figure 9 shows corresponding spiral-out-in results, which exhibit strongly distinct contrast due to the discrepancy in echo time (3 ms vs 40 ms). At the short TE, residual fat signal from the scalp gives rise to slight ringing. With the spiral-in readout, off-resonance correction still achieves good integrity of depiction despite very late acquisition of central k-space.

Discussion

The results of this study show that single-shot spiral acquisition is a viable means of boosting encoding speed for high-field brain imaging. Competitive image quality has been achieved by inversion of an expanded signal model that jointly accounts for static off-resonance, actual k-space trajectories, zeroth-order field dynamics, and sensitivity encoding with a receiver array. With this approach, extended readouts of 53 ms have been found to be robust at 7T, encoding nominal in-plane resolution of 0.8 mm in a single shot. These specifications are remarkable in that they exceed those previously reported for spiral imaging at 3T, despite worse B_0 uniformity at higher field.

Rapid high-resolution readouts leverage the SNR advantage of high field, which makes them attractive for a range of applications. Sub-millimeter resolution by single shots is especially attractive for BOLD fMRI time series. In this study, T_2*- weighted data still featured visually appealing sensitivity even at 1 mm slice thickness and thus at a sub-µl voxel volume. Another promising application is ASL, which typically targets somewhat lower resolution but benefits particularly from the combination of high acquisition duty cycle and the short echo time that spirals offer. These features are equally desired in diffusion-weighted scanning, which is also increasingly explored at high field (55,56).

As illustrated in the second part of this study, extended spiral readouts can also be used to acquire two images after a single excitation in what may be called a half-shot strategy. This approach was pioneered in fMRI, particularly for physiological noise correction (57) and multi-echo combination (10,58), and has also been used for joint water-fat estimation (59,60). Two successive spiral readouts may also be of different length and k-space range. In particular, a leading or trailing low-resolution spiral could serve for supporting purposes such as navigation or $\Delta\omega_0$ and coil sensitivity mapping. Finally, good quality of depiction with single-shot 2D spirals suggests that other long and non-Cartesian readouts, particularly 3D and multi-band spirals (59,61,62) may hold promise for similar levels of robustness.

As observed in the PSF study, T_2* decay during the spiral readout causes actual resolution in gray and white matter to fall somewhat short of the nominal values. If considered limiting, this type of resolution loss could be countered at the raw data level by compensatory multiplication with the inverse of a decay exponential, assuming some intermediate global T_2* value. With this approach, PSF broadening for short- T_2* tissue will be mitigated while over-sharpening the PSF of long- T_2* material, particularly of cerebrospinal fluid. Boosting attenuated data in this way must be done with moderation to limit the amplification also of noise and of PSF sidelobes for long- T_2* material, which will appear as ringing. Alternatively, when leaving the raw data uncompensated as done here, the T_2* decay has the same effect as common ringing filters, which also attenuate PSF sidelobes at some expense in resolution. Importantly, actual resolution in brain as a function of readout duration was found to still exhibit a significant slope at the reported acquisition time of 53 ms. This indicates that moving to readouts of such length does pay off in terms of resolution and even somewhat longer acquisition may still add to image quality.

Good quality of depiction reflects suitability of the signal model and all constituents of the model have been found to be essential for the single-shot case (Fig. 5). However, limitations to the model remain. Most prominently, in the form used here it does not describe intra-voxel field variation. Therefore, in-plane and through-plane dephasing in regions with strong static field gradients remain unaddressed. This applies to the area of the ear canals, the orbits, the nasal cavities and, in the case shown, to a calcification between the frontal lobes (Fig. 4). Signal dropout may partly be countered by exciting thinner slices, yet at the expense of SNR. Enhancing the signal model towards intra-voxel description is straightforward per se and an interesting option but will render the inverse problem ill-conditioned. With regard to readout strategies it is important to note that dephasing issues are not specific to spiral scans but rather inherent to long readout schemes.

Irrespective of model-inherent constraints, depiction quality is also limited by the finite accuracy of the model ingredients. Strong local field variation introduces error also in $\Delta\omega_0$ mapping, which is manifest as residual blurring and distortion in the same critical regions as mentioned above (lower slices in Figure 4). When disregarding $\Delta\omega_0$, similar artifacts appear to a greater extent and in all brain regions (Fig. 6). The fidelity of $\Delta\omega_0$ and coil sensitivity maps is also impaired by motion between the mapping scan and subsequent spiral scans. $\Delta\omega_0$ maps tend to be more critical in this respect. This is partly due to their finer structure, especially at the interfaces between brain tissue, skull, scalp and air. In addition, off-resonance is caused mostly by tissue susceptibility and thus changes strongly as the head moves. In contrast, coil sensitivity reflects primarily coil geometry and is influenced more indirectly by changes in load upon motion. When limiting, geometric congruency between different scans can generally be improved by motion tracking with navigators (63), optical cameras (64) or field probes (65,66). However, since both susceptibility and RF effects are orientation-dependent, large motion will still be limiting. The need to map $\Delta\omega_0$ and coil sensitivity in the first place also takes additional time. In the present work, a robust, high-resolution scan of 5 min was used for this purpose and no effort was made to minimize the time burden. There is scope for reducing it, however, by faster imaging techniques and compromising on spatial resolution.

The third model ingredient, field dynamics, can be determined by a range of methods. Spiral trajectories have previously been mapped using additional reference scans on a phantom or the subject itself (24,67–69). More recently they have also been predicted based on gradient impulse response functions (41,70,71). In the present work, field dynamics were recorded with NMR probes, which is convenient in that it can be performed concurrently with actual imaging and will capture potential system drifts and other transient effects. In previous studies, magnet drift and heating of gradient coils have been identified as relevant system changes, giving rise to image variation up to several percent in EPI (18,72). Differences between trajectory prediction based on impulse response and concurrent trajectory recording were also reported in (41), resulting in RMS image differences of approximately 2% for single-shot spiral imaging.

While all imaging in this work was in transverse orientation, the field sensing and reconstruction approaches hold unaltered for arbitrary slice angulation (41). The level of gradient fidelity and feasibility of correction at the reconstruction stage do not commonly vary greatly with slice geometry. However, differences in static off-resonance and through-plane gradients will cause some dependence of image quality on slice position and orientation. The relaxation times and droplet size of the field probes determine the feasible specifications of spiral readouts as well as the maximum rate of probe re-excitation. At a droplet diameter of 0.8 mm the probes used here support imaging down to resolutions of approximately 0.4 mm (25), which is amply sufficient for the single-shot

scenario. At the used probe T_2* of 24 ms, probe readouts could not be extended much beyond the durations used in this work. Longer spiral acquisition could be readily supported, however, with probes doped for longer signal lifetime.

An important challenge that comes with expanding the signal model is increased computation for model inversion. Readout duration is a key determinant of reconstruction time since it co-defines the number of frequency segments required for multiple frequency interpolation. For the longest readouts of 53 ms, reconstruction times ranged up to 10s of seconds per image. However, exploring feasibility, no efforts have been undertaken to render reconstruction particularly efficient. Towards routine use, there is substantial scope for acceleration by basic algorithmic optimization as well as distribution on ever larger CPU or GPU clusters (73).

References

1. Ahn CB, Kim JH, Cho ZH. High-Speed Spiral-Scan Echo Planar NMR Imaging-I. IEEE Trans. Med. Imaging 1986;5:2–7. doi: 10.1109/TMI.1986.4307732.

2. Meyer CH, Hu BS, Nishimura DG, Macovski A. Fast Spiral Coronary Artery Imaging. Magn. Reson. Med. 1992;28:202–213. doi: 10.1002/mrm.1910280204.

3. Börnert P, Schomberg H, Aldefeld B, Groen J. Improvements in spiral MR imaging. Magn. Reson. Mater. Phys. Biol. Med. 1999;9:29–41. doi: 10.1007/BF02634590.

4. Glover GH, Lai S. Self-navigated spiral fMRI: Interleaved versus single-shot. Magn. Reson. Med. 1998;39:361–368. doi: 10.1002/mrm.1910390305.

5. Nishimura DG, Irarrazabal P, Meyer CH. A Velocity k-Space Analysis of Flow Effects in Echo-Planar and Spiral Imaging. Magn. Reson. Med. 1995;33:549–556. doi: 10.1002/mrm.1910330414.

6. Liu C, Bammer R, Kim D, Moseley ME. Self-navigated interleaved spiral (SNAILS): Application to high-resolution diffusion tensor imaging. Magn. Reson. Med. 2004;52:1388–1396. doi: 10.1002/mrm.20288.

7. Wilm BJ, Barmet C, Gross S, Kasper L, Vannesjo SJ, Haeberlin M, Dietrich BE, Brunner DO, Schmid T, Pruessmann KP. Single-shot spiral imaging enabled by an expanded encoding model: Demonstration in diffusion MRI. Magn. Reson. Med. 2017;77:83–91. doi: 10.1002/mrm.26493.

8. Meyer CH, Zhao L, Lustig M, Jilwan-Nicolas M, Wintermark M, Mugler JP, Epstein FH. Dual-density and parallel spiral ASL for motion artifact reduction. In: Proc. Intl. Soc. Mag. Reson. Med. Vol. 19. ; 2011. p. 3986.

9. Noll DC, Cohen JD, Meyer CH, Schneider W. Spiral K-space MR imaging of cortical activation. J. Magn. Reson. Imaging 1995;5:49–56. doi: 10.1002/jmri.1880050112.

10. Glover GH, Law CS. Spiral-in/out BOLD fMRI for increased SNR and reduced susceptibility artifacts. Magn. Reson. Med. 2001;46:515–522. doi: 10.1002/mrm.1222.

11. Jung Y, Samsonov AA, Liu TT, Buracas GT. High efficiency multishot interleaved spiral-in/out: Acquisition for high-resolution BOLD fMRI. Magn. Reson. Med. 2013;70:420–428. doi: 10.1002/mrm.24476.

12. Block KT, Frahm J. Spiral imaging: A critical appraisal. J. Magn. Reson. Imaging 2005;21:657–668. doi: 10.1002/jmri.20320.

13. Boesch C, Gruetter R, Martin E. Temporal and spatial analysis of fields generated by eddy currents in superconducting magnets: Optimization of corrections and quantitative characterization of magnet/gradient systems. Magn. Reson. Med. 1991;20:268–284. doi: 10.1002/mrm.1910200209.

14. Liu Q, Hughes DG, Allen PS. Quantitative characterization of the eddy current fields in a 40-cm bore superconducting magnet. Magn. Reson. Med. 1994;31:73–76. doi: 10.1002/mrm.1910310112.

15. Bernstein MA, Zhou XJ, Polzin JA, King KF, Ganin A, Pelc NJ, Glover GH. Concomitant gradient terms in phase contrast MR: Analysis and correction. Magn. Reson. Med. 1998;39:300–308. doi: 10.1002/mrm.1910390218.

16. Aldefeld B, Börnert P. Effects of gradient anisotropy in MRI. Magn. Reson. Med. 1998;39:606–614. doi: 10.1002/mrm.1910390414.

17. Busch J, Vannesjo SJ, Barmet C, Pruessmann KP, Kozerke S. Analysis of temperature dependence of background phase errors in phase-contrast cardiovascular magnetic resonance. J. Cardiovasc. Magn. Reson. [Internet] 2014;16. doi: 10.1186/s12968-014-0097-6.

18. Kasper L, Bollmann S, Vannesjo SJ, Gross S, Haeberlin M, Dietrich BE, Pruessmann KP. Monitoring, analysis, and correction of magnetic field fluctuations in echo planar imaging time series: Magnetic Field Fluctuations in EPI. Magn. Reson. Med. 2015;74:396–409. doi: 10.1002/mrm.25407.

19. Wu Y, Chronik BA, Bowen C, Mechefske CK, Rutt BK. Gradient-induced acoustic and magnetic field fluctuations in a 4T whole-body MR imager. Magn. Reson. Med. 2000;44:532–536. doi: 10.1002/1522-2594(200010)44:4<532::AID-MRM6>3.0.CO;2-Q.

20. Van de Moortele P-F, Pfeuffer J, Glover GH, Ugurbil K, Hu X. Respiration-induced B0 fluctuations and their spatial distribution in the human brain at 7 Tesla. Magn. Reson. Med. 2002;47:888–895. doi: 10.1002/mrm.10145.

21. Versluis MJ, Peeters JM, van Rooden S, van der Grond J, van Buchem MA, Webb AG, van Osch MJP. Origin and reduction of motion and f0 artifacts in high resolution T2*-weighted magnetic resonance imaging: Application in Alzheimer's disease patients. NeuroImage 2010;51:1082–1088. doi: 10.1016/j.neuroimage.2010.03.048.

22. Vannesjo SJ, Wilm BJ, Duerst Y, Gross S, Brunner DO, Dietrich BE, Schmid T, Barmet C, Pruessmann KP. Retrospective correction of physiological field fluctuations in high-field brain MRI using concurrent field monitoring: Physiological Field Correction Using Concurrent Field Monitoring. Magn. Reson. Med. 2015;73:1833–1843. doi: 10.1002/mrm.25303.

23. Morich MA, Lampman DA, Dannels WR, Goldie FTD. Exact temporal eddy current compensation in magnetic resonance imaging systems. IEEE Trans. Med. Imaging 1988;7:247–254. doi: 10.1109/42.7789.

24. Duyn JH, Yang Y, Frank JA, van der Veen JW. Simple Correction Method for k-Space Trajectory Deviations in MRI. J. Magn. Reson. 1998;132:150–153. doi: 10.1006/jmre.1998.1396.

25. Barmet C, Zanche ND, Pruessmann KP. Spatiotemporal magnetic field monitoring for MR. Magn. Reson. Med. 2008;60:187–197. doi: 10.1002/mrm.21603.

26. Wilm BJ, Barmet C, Pavan M, Pruessmann KP. Higher order reconstruction for MRI in the presence of spatiotemporal field perturbations. Magn. Reson. Med. 2011;65:1690–1701. doi: 10.1002/mrm.22767.

27. Yudilevich E, Stark H. Spiral sampling in magnetic resonance imaging – the effect of inhomogeneities. IEEE Trans. Med. Imaging 1987;6:337–345. doi: 10.1109/TMI.1987.4307852.

28. Pruessmann KP, Weiger M, Börnert P, Boesiger P. Advances in sensitivity encoding with arbitrary k-space trajectories. Magn. Reson. Med. 2001;46:638–651. doi: 10.1002/mrm.1241.

29. Weiger M, Pruessmann KP, Österbauer R, Börnert P, Boesiger P, Jezzard P. Sensitivity-encoded single-shot spiral imaging for reduced susceptibility artifacts in BOLD fMRI: Sensitivity-Encoded Spiral BOLD fMRI. Magn. Reson. Med. 2002;48:860–866. doi: 10.1002/mrm.10286.

30. Yeh EN, Stuber M, McKenzie CA, Botnar RM, Leiner T, Ohliger MA, Grant AK, Willig-Onwuachi JD, Sodickson DK. Inherently self-calibrating non-cartesian parallel imaging. Magn. Reson. Med. 2005;54:1–8. doi: 10.1002/mrm.20517.

31. Heberlein and K, Hu X. Auto-calibrated parallel spiral imaging. Magn. Reson. Med. 2006;55:619–625. doi: 10.1002/mrm.20811.

32. Heidemann RM, Griswold MA, Seiberlich N, Krüger G, Kannengiesser SAR, Kiefer B, Wiggins G, Wald LL, Jakob PM. Direct parallel image reconstructions for spiral trajectories using GRAPPA. Magn. Reson. Med. 2006;56:317–326. doi: 10.1002/mrm.20951.

33. Maeda A, Sano K, Yokoyama T. Reconstruction by weighted correlation for MRI with time-varying gradients. IEEE Trans. Med. Imaging 1988;7:26–31. doi: 10.1109/42.3926.

34. Noll DC, Meyer CH, Pauly JM, Nishimura DG, Macovski A. A homogeneity correction method for magnetic resonance imaging with time-varying gradients. IEEE Trans. Med. Imaging 1991;10:629–637. doi: 10.1109/42.108599.

35. Noll DC, Pauly JM, Meyer CH, Nishimura DG, Macovski A. Deblurring for non-2D Fourier transform magnetic resonance imaging. Magn. Reson. Med. 1992;25:319–333.

36. Man L-C, Pauly JM, Macovski A. Multifrequency interpolation for fast off-resonance correction. Magn. Reson. Med. 1997;37:785–792. doi: 10.1002/mrm.1910370523.

37. Harshbarger TB, Twieg DB. Iterative reconstruction of single-shot spiral MRI with off resonance. IEEE Trans. Med. Imaging 1999;18:196–205. doi: 10.1109/42.764889.

38. Sutton BP, Noll DC, Fessler JA. Fast, iterative image reconstruction for MRI in the presence of field inhomogeneities. IEEE Trans. Med. Imaging 2003;22:178–188. doi: 10.1109/TMI.2002.808360.

39. Barmet C, Tsao J, Pruessmann KP. Efficient iterative reconstruction for parallel MRI in strongly inhomogeneous B0. In: Proceedings of the 13th Annual Meeting of ISMRM, Miami. ; 2004. p. 347.

40. Barmet C, Tsao J, Pruessmann KP. Sensitivity encoding and B0 inhomogeneity – A simultaneous reconstruction approach. In: Proceedings of the ISMRM. ; 2005. p. 682.

41. Vannesjo SJ, Graedel NN, Kasper L, Gross S, Busch J, Haeberlin M, Barmet C, Pruessmann KP. Image reconstruction using a gradient impulse response model for trajectory prediction. Magn. Reson. Med. 2016;76:45–58. doi: 10.1002/mrm.25841.

42. Goense J, Bohraus Y, Logothetis NK. fMRI at High Spatial Resolution: Implications for BOLD-Models. Front. Comput. Neurosci. [Internet] 2016;10. doi: 10.3389/fncom.2016.00066.

43. Ivanov D, Gardumi A, Haast RAM, Pfeuffer J, Poser BA, Uludağ K. Comparison of 3T and 7T ASL techniques for concurrent functional perfusion and BOLD studies. NeuroImage 2017;156:363–376. doi: 10.1016/j.neuroimage.2017.05.038.

44. Qian Y, Zhao T, Hue Y-K, Ibrahim TS, Boada FE. High-resolution spiral imaging on a whole-body 7T scanner with minimized image blurring. Magn. Reson. Med. 2010;63:543–552. doi: 10.1002/mrm.22215.

45. Kasper L, Engel M, Barmet C, et al. Rapid anatomical brain imaging using spiral acquisition and an expanded signal model. NeuroImage [Internet] 2017. doi: 10.1016/j.neuroimage.2017.07.062.

46. Mason GF, Harshbarger T, Hetherington HP, Zhang Y, Pohost GM, Twieg DB. A Method to measure arbitrary k-space trajectories for rapid MR imaging. Magn. Reson. Med. 1997;38:492–496. doi: 10.1002/mrm.1910380318.

47. De Zanche N, Barmet C, Nordmeyer-Massner JA, Pruessmann KP. NMR probes for measuring magnetic fields and field dynamics in MR systems. Magn. Reson. Med. 2008;60:176–186. doi: 10.1002/mrm.21624.

48. Gross S, Barmet C, Dietrich BE, Brunner DO, Schmid T, Pruessmann KP. Dynamic nuclear magnetic resonance field sensing with part-per-trillion resolution. Nat. Commun. 2016;7:13702. doi: 10.1038/ncomms13702.

49. Dietrich BE, Brunner DO, Wilm BJ, Barmet C, Gross S, Kasper L, Haeberlin M, Schmid T, Vannesjo SJ, Pruessmann KP. A field camera for MR sequence monitoring and system analysis. Magn. Reson. Med. 2016;75:1831–1840. doi: 10.1002/mrm.25770.

50. Lustig M, Kim S-J, Pauly JM. A Fast Method for Designing Time-Optimal Gradient Waveforms for Arbitrary k-Space Trajectories. IEEE Trans. Med. Imaging 2008;27:866–873. doi: 10.1109/TMI.2008.922699.

51. Kaldoudi E, Williams SCR, Barker GJ, Tofts PS. A chemical shift selective inversion recovery sequence for fat-suppressed MRI: Theory and experimental validation. Magn. Reson. Imaging 1993;11:341–355. doi: 10.1016/0730-725X(93)90067-N.

52. Keeling SL, Bammer R. A variational approach to magnetic resonance coil sensitivity estimation. Appl. Math. Comput. 2004;158:359–388. doi: 10.1016/j.amc.2003.08.110.

53. Ashburner J, Friston KJ. Unified segmentation. NeuroImage 2005;26:839–851. doi: 10.1016/j.neuroimage.2005.02.018.

54. Peters AM, Brookes MJ, Hoogenraad FG, Gowland PA, Francis ST, Morris PG, Bowtell R. T2* measurements in human brain at 1.5, 3 and 7 T. Magn. Reson. Imaging 2007;25:748–753. doi: 10.1016/j.mri.2007.02.014.

55. Heidemann RM, Porter DA, Anwander A, Feiweier T, Heberlein K, Knösche TR, Turner R. Diffusion imaging in humans at 7T using readout-segmented EPI and GRAPPA. Magn. Reson. Med. 2010;64:9–14. doi: 10.1002/mrm.22480.

56. In M-H, Posnansky O, Speck O. PSF mapping-based correction of eddy-current-induced distortions in diffusion-weighted echo-planar imaging: Correction of Distortions in DW-EPI. Magn. Reson. Med. 2016;75:2055–2063. doi: 10.1002/mrm.25746.

57. Kundu P, Inati SJ, Evans JW, Luh W-M, Bandettini PA. Differentiating BOLD and non-BOLD signals in fMRI time series using multi-echo EPI. NeuroImage 2012;60:1759–1770. doi: 10.1016/j.neuroimage.2011.12.028.

58. Glover GH, Thomason ME. Improved combination of spiral-in/out images for BOLD fMRI. Magn. Reson. Med. 2004;51:863–868. doi: 10.1002/mrm.20016.

59. Li Z, Wang D, Robison RK, Zwart NR, Schär M, Karis JP, Pipe JG. Sliding-slab three-dimensional TSE imaging with a spiral-In/Out readout: Sliding-Slab Spiral TSE. Magn. Reson. Med. 2016;75:729–738. doi: 10.1002/mrm.25660.

60. Wang D, Zwart NR, Li Z, Schär M, Pipe JG. Analytical three-point Dixon method: With applications for spiral water-fat imaging: Analytical Three-Point Dixon Method. Magn. Reson. Med. 2016;75:627–638. doi: 10.1002/mrm.25620.

61. Zahneisen B, Poser BA, Ernst T, Stenger AV. Simultaneous Multi-Slice fMRI using spiral trajectories. NeuroImage 2014;92:8–18. doi: 10.1016/j.neuroimage.2014.01.056.

62. Zahneisen B, Poser BA, Ernst T, Stenger VA. Three-dimensional Fourier encoding of simultaneously excited slices: Generalized acquisition and reconstruction framework. Magn. Reson. Med. 2014;71:2071–2081. doi: 10.1002/mrm.24875.

63. Lee CC, Jack CR, Grimm RC, Rossman PJ, Felmlee JP, Ehman RL, Riederer SJ. Real-time adaptive motion correction in functional MRI. Magn. Reson. Med. 1996;36:436–444. doi: 10.1002/mrm.1910360316.

64. Zaitsev M, Dold C, Sakas G, Hennig J, Speck O. Magnetic resonance imaging of freely moving objects: prospective real-time motion correction using an external optical motion tracking system. NeuroImage 2006;31:1038–1050. doi: 10.1016/j.neuroimage.2006.01.039.

65. Ooi MB, Krueger S, Thomas WJ, Swaminathan SV, Brown TR. Prospective real-time correction for arbitrary head motion using active markers. Magn. Reson. Med. 2009;62:943–954. doi: 10.1002/mrm.22082.

66. Haeberlin M, Kasper L, Barmet C, Brunner DO, Dietrich BE, Gross S, Wilm BJ, Kozerke S, Pruessmann KP. Real-time motion correction using gradient tones and head-mounted NMR field probes. Magn. Reson. Med. 2015;74:647–660. doi: 10.1002/mrm.25432.

67. Alley MT, Glover GH, Pelc NJ. Gradient characterization using a Fourier-transform technique. Magn. Reson. Med. 1998;39:581–587. doi: 10.1002/mrm.1910390411.

68. Tan H, Meyer CH. Estimation of k-space trajectories in spiral MRI. Magn. Reson. Med. 2009;61:1396–1404. doi: 10.1002/mrm.21813.

69. Robison RK, Devaraj A, Pipe JG. Fast, simple gradient delay estimation for spiral MRI. Magn. Reson. Med. 2010;63:1683–1690. doi: 10.1002/mrm.22327.

70. Addy NO, Wu HH, Nishimura DG. A Simple Method for MR Gradient System Characterization and k-Space Trajectory Estimation. Magn. Reson. Med. 2012;68:120–129. doi: 10.1002/mrm.23217.

71. Vannesjo SJ, Haeberlin M, Kasper L, Pavan M, Wilm BJ, Barmet C, Pruessmann KP. Gradient system characterization by impulse response measurements with a dynamic field camera. Magn. Reson. Med. 2013;69:583–593. doi: 10.1002/mrm.24263.

72. Bollmann S, Kasper L, Vannesjo SJ, Diaconescu AO, Dietrich BE, Gross S, Stephan KE, Pruessmann KP. Analysis and correction of field fluctuations in fMRI data using field monitoring. NeuroImage 2017;154:92–105. doi: 10.1016/j.neuroimage.2017.01.014.

73. Xue H, Inati S, Sørensen TS, Kellman P, Hansen MS. Distributed MRI reconstruction using gadgetron-based cloud computing: Gadgetron C-Bud Computing. Magn. Reson. Med. 2015;73:1015–1025. doi: 10.1002/mrm.25213.

Fig. 1: Setup for concurrent field monitoring: NMR field probes (black) are placed at suitable positions between the receive array and the surrounding transmitter, which slides over the receive part for operation.

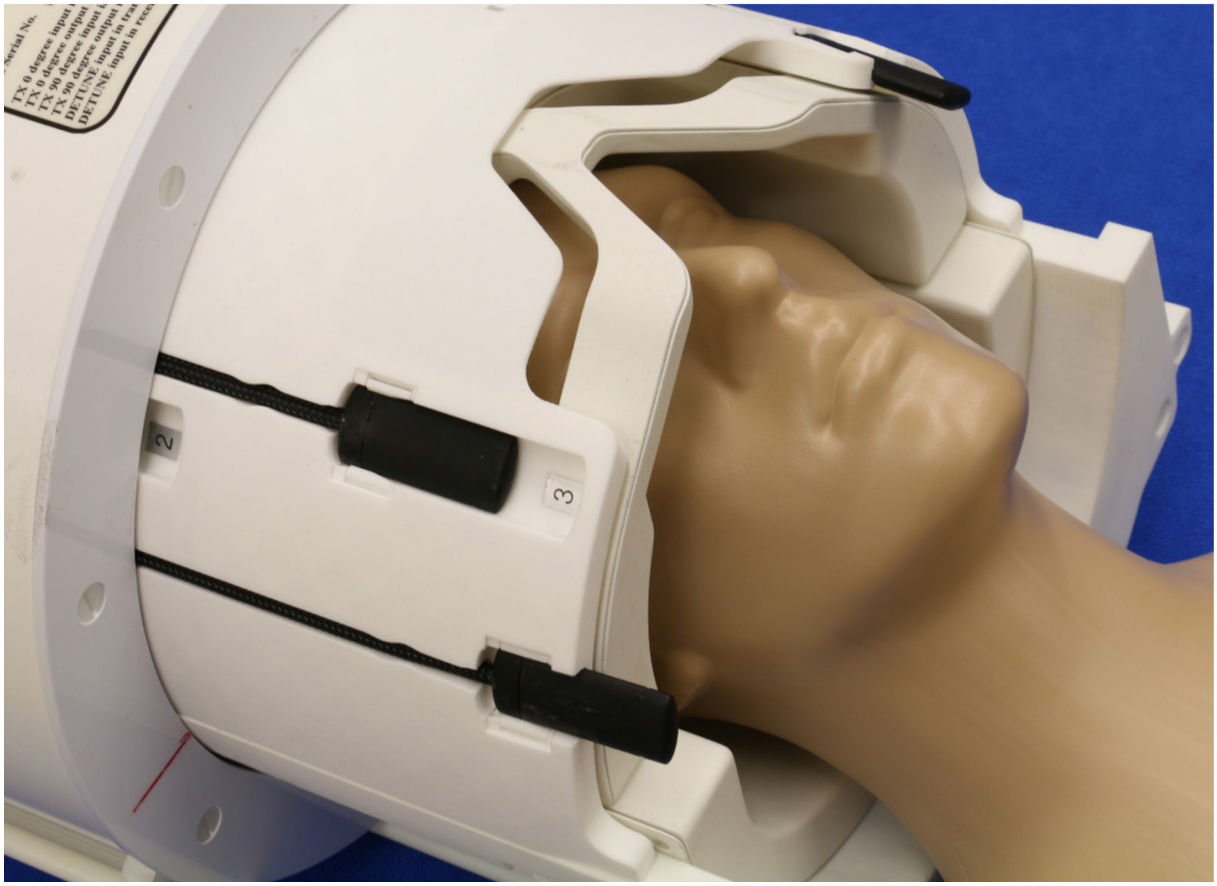

Fig. 2: Diagram of the gradient echo sequences used in this work. Orange: single-shot spiral-out acquisition. Green: spiral-in-out and spiral-out-in trajectories that read out two images successively ('half-shot'). Solid and dashed lines plot G_x and G_y, respectively. Field probes are excited before the respective spiral waveform and then read out concurrently with head-coil acquisition.

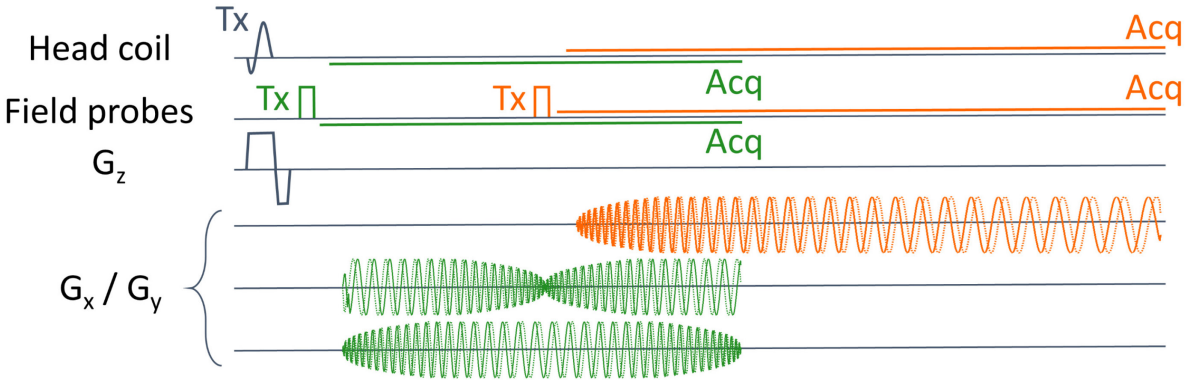

Tab. 1: Sequence parameters.

Readout trajectory	Spiral-out	Spiral-in-out	Spiral-out-in
Resolution [mm]	0.8	1.50	1.50
FOV [cm]	23	23	23
Undersampling factor R	4	4	4
Echotime TE [ms]	25	22/22	3/40
Readout time [ms]	53	2*18.5	2*18.5
# slices	36	36	36
Slice thickness [mm]	1, 2	2	2
Slice gap [mm]	2.5, 1.5	1.5	1.5

Fig. 3: Off-resonance maps for central slices. Left: first subject (Figures 4, 6). Right: second subject (Figures 8, 9).

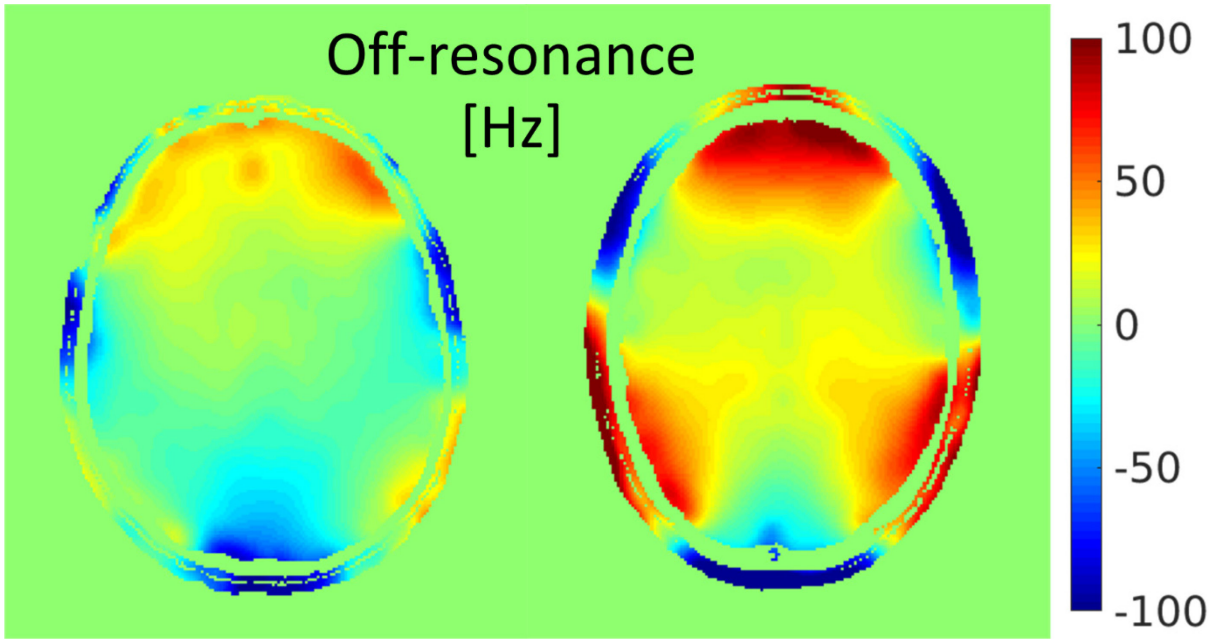

Fig. 4: Spiral-out imaging with TE = 25 ms, 0.8 mm nominal resolution. The bottom panel displays the central 27 of 36 slices at 1 mm slice thickness. Five selected slices are shown magnified for closer inspection and comparison with thicker slices (2 mm).

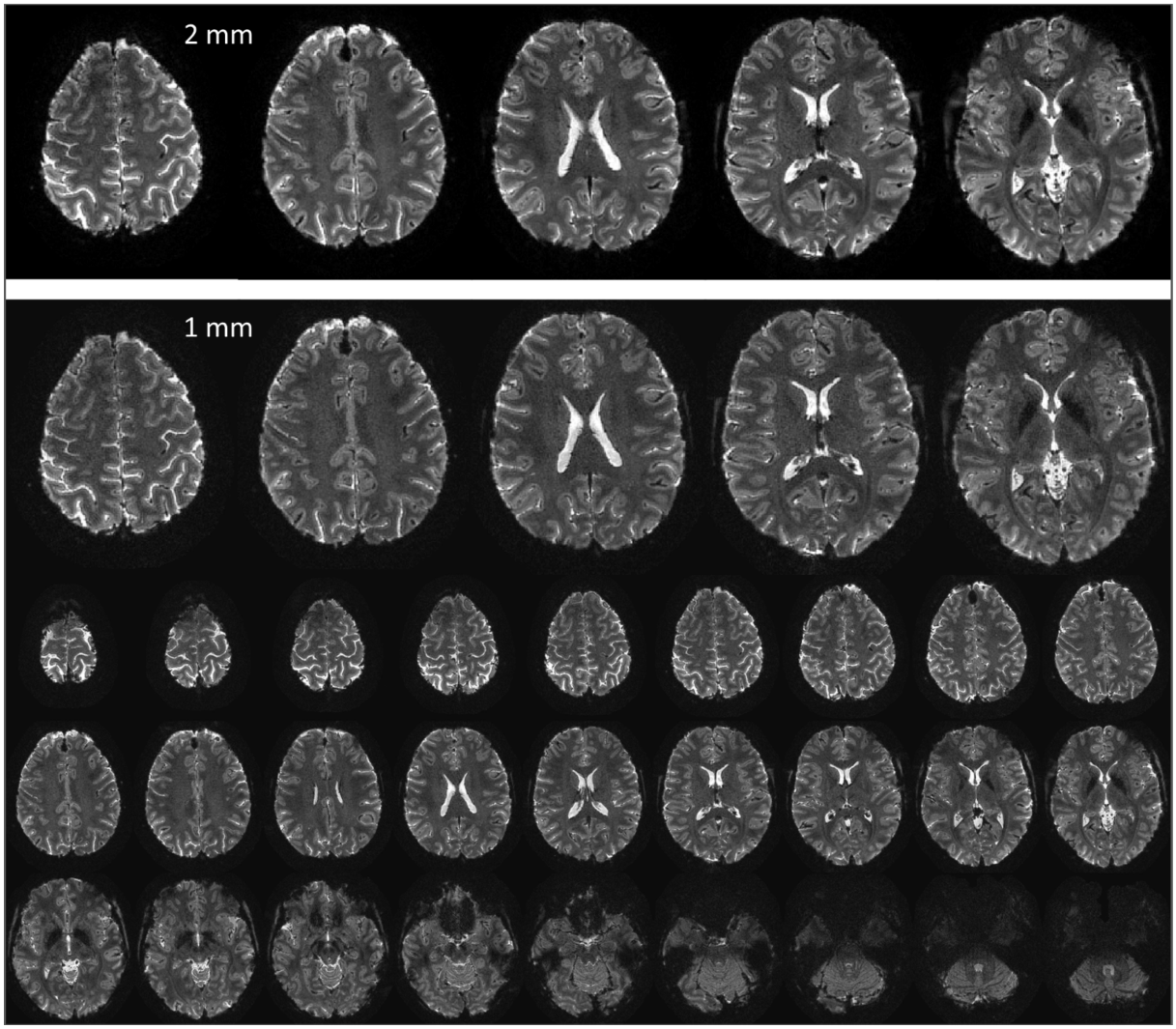

Fig. 5: Monitored field dynamics in terms of ^{1}H phase accrual, expanded into spherical harmonics of 0^{th} to 2^{nd} order (top to bottom). The first-order terms are the common k-space coordinates. Plots are scaled to show maximum phase excursion in [rad] within a sphere of 10 cm diameter. Note the different scaling of the vertical axis for the 1^{st}-order terms (left).

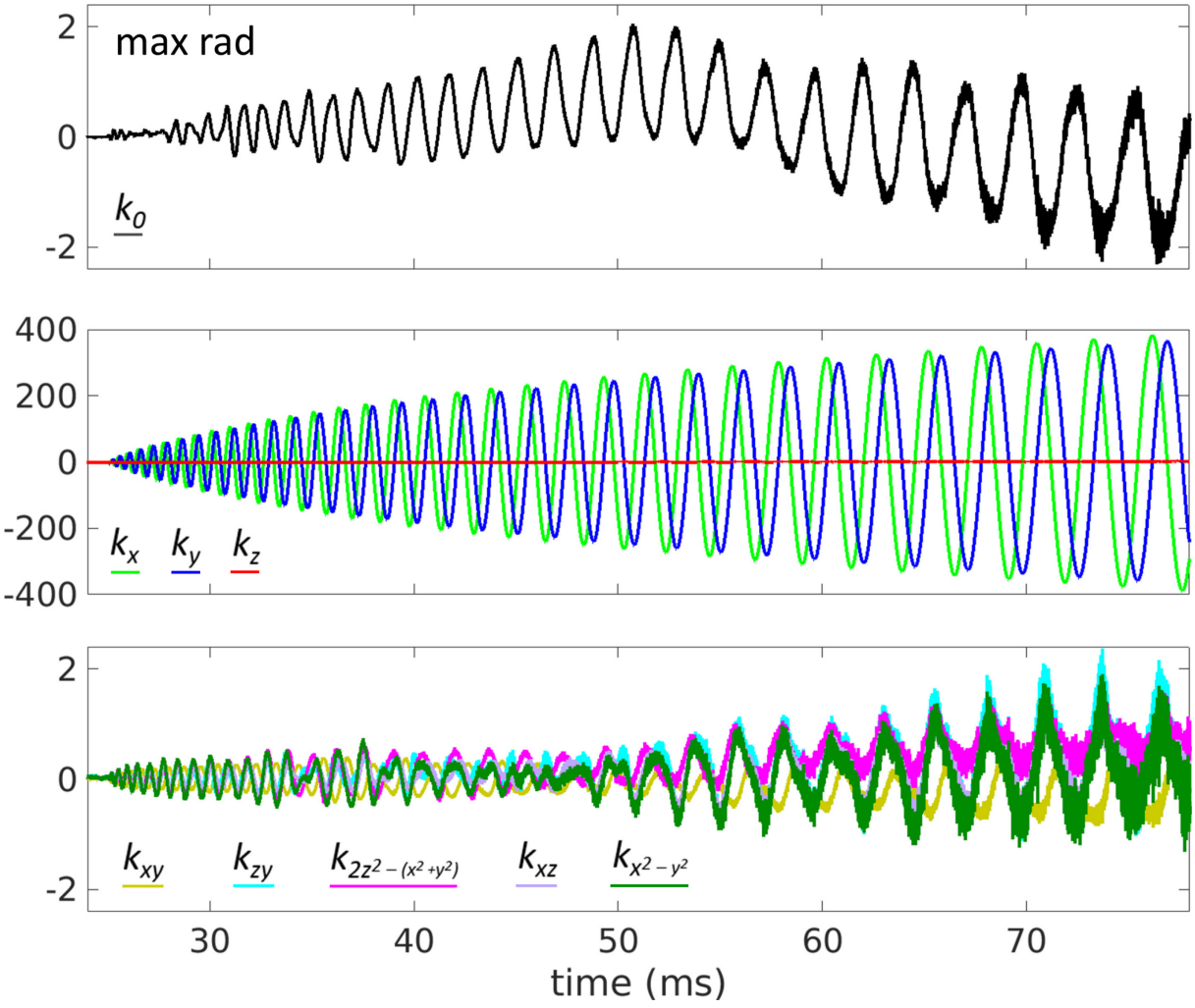

Fig. 6: Impact of signal model constituents, shown for a 1 mm slice selected from Fig. 4. The four images in the left panel were reconstructed from four successive spiral shots, amounting to full-density k-space sampling. Image reconstruction was performed with and without accounting for static and measured dynamic field as indicated. The right panel shows the single-shot case (4x undersampling), relying on the coil sensitivity terms in the signal model in addition to $\Delta\omega_0$ (Fig. 3, left) and the measured trajectory (Fig. 5).

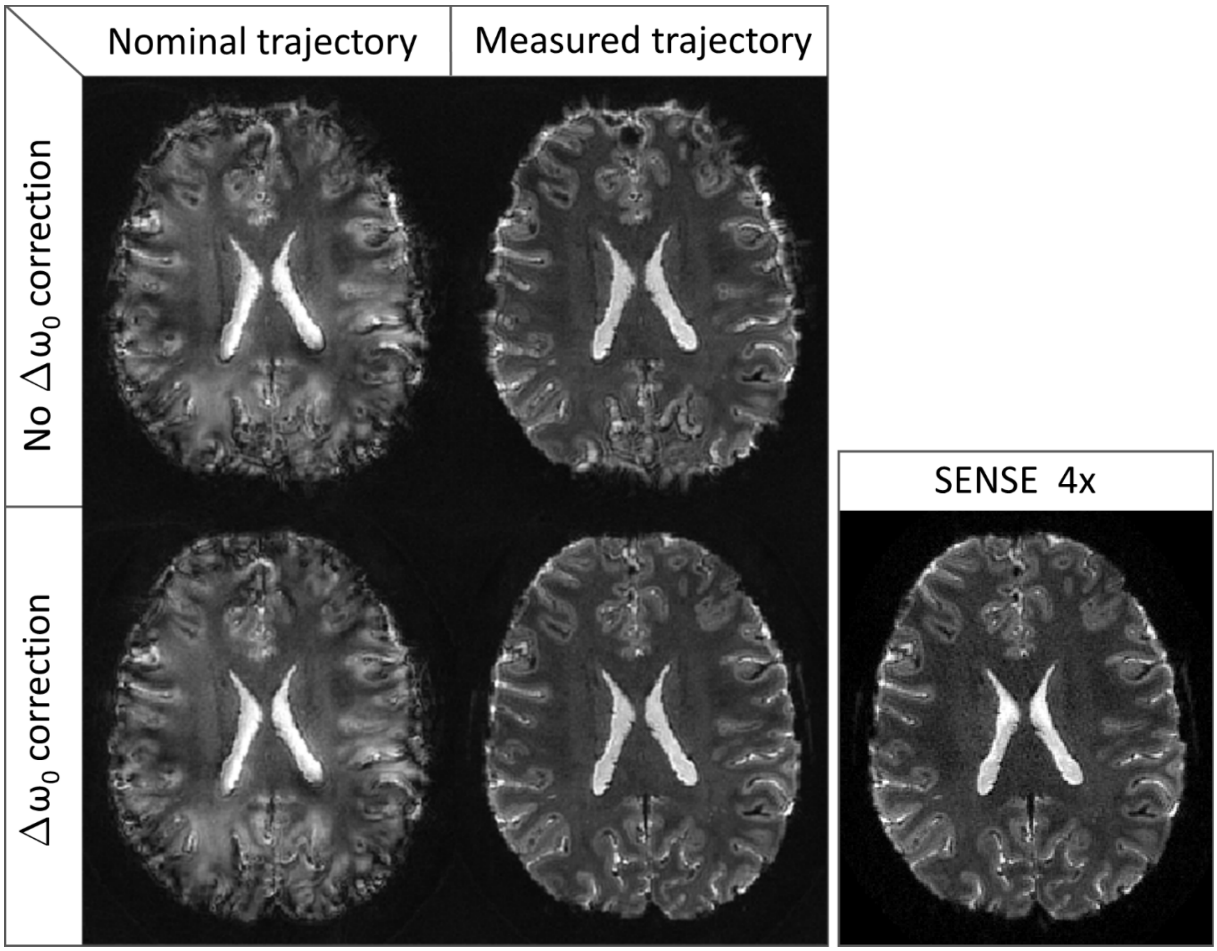

Fig. 7: Effect of T_2* decay on image resolution and the equivalent full width at half-maximum (FWHM) of the PSF. Red: nominal resolution obtained with the single-shot spiral-out approach as a function of acquisition duration. Blue, yellow: actual resolution in the presence of T_2* decay as encountered in gray and white matter, respectively.

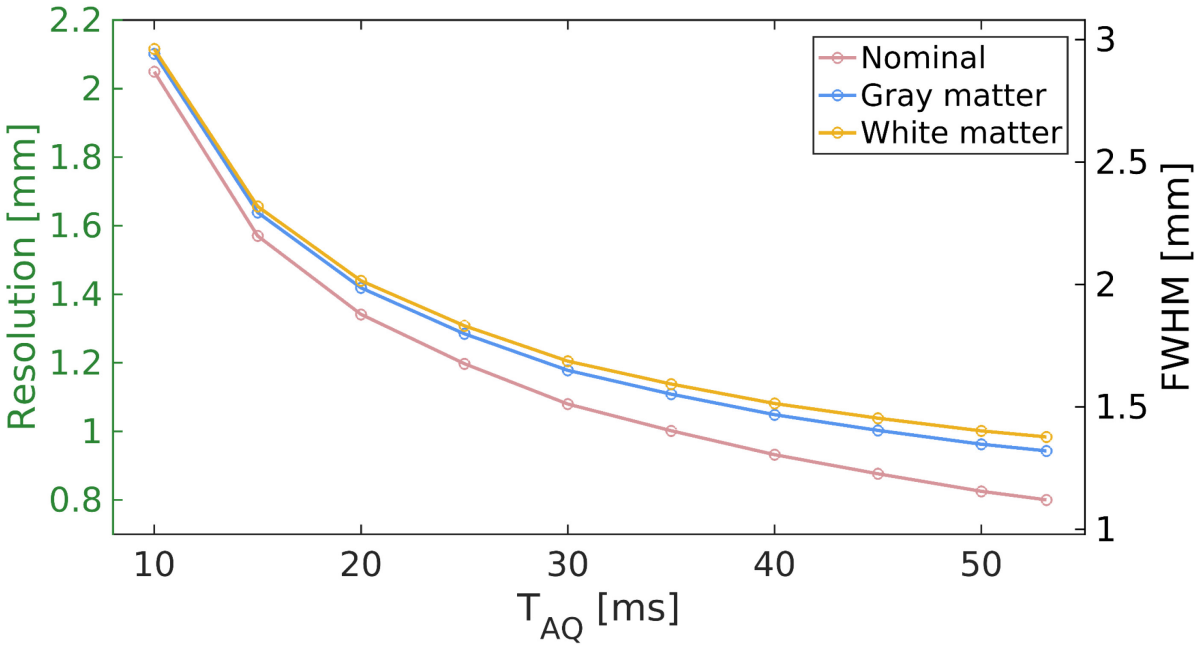

Fig. 8: Spiral-in-out: Reconstruction results for five selected slices and the underlying recorded trajectory (0^{th} and 1^{st} order). A) Spiral-in and B) spiral-out images.

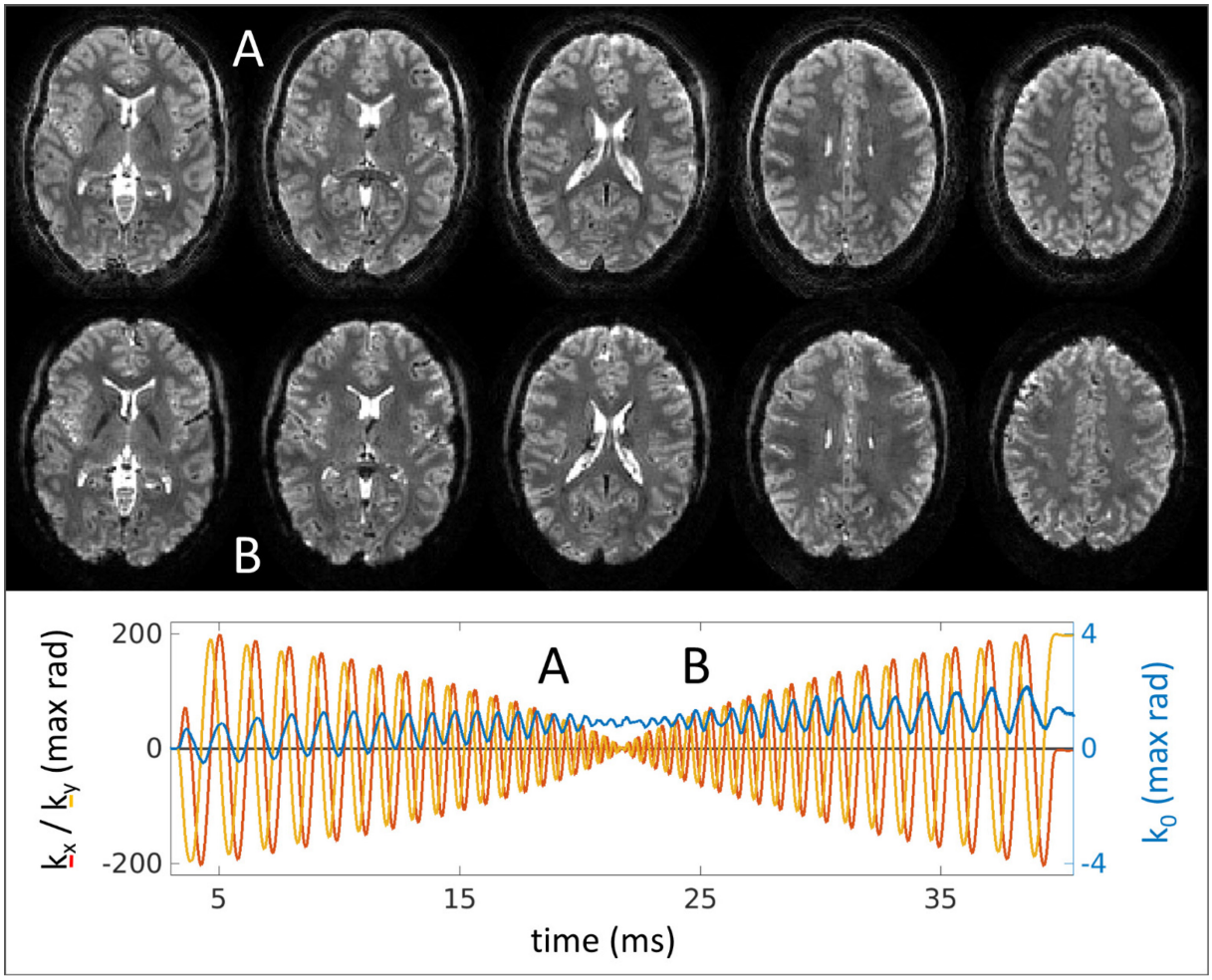

Fig. 9: Spiral-out-in: Reconstruction results for five selected slices and the underlying recorded trajectory (0^{th} and 1^{st} order). A) Spiral-out and B) spiral-in images.